ACS APPLIED MATERIALS & INTERFACES

Biological and Medical Applications of Materials and Interfaces

Defect and Additional Active Sites on the Basal Plane of Manganese Doped Molybdenum Diselenide for Effective Enzyme Immobilization: In-vitro and In-vivo Real Time Analysis for Hydrogen Peroxide Sensing

Sukanya Ramaraj, Mani Sakthivel, Shen-Ming Chen, Bih-Show Lou, and Kuo-Chuan Ho

ACS Appl. Mater. Interfaces, **Just Accepted Manuscript** • DOI: 10.1021/acsami.8b22389 • Publication Date (Web): 30 Jan 2019

Just Accepted

ACS Publications

is published by the American Chemical Society. 1155 Sixteenth Street N.W., Washington, DC 20036

Defect and Additional Active Sites on the Basal Plane of Manganese Doped Molybdenum Diselenide for Effective Enzyme Immobilization: In-vitro and In-vivo Real Time Analysis for Hydrogen Peroxide Sensing

Sukanya Ramaraj[a], Mani Sakthivel[b,c], Shen-Ming Chen[a]*, Bih-Show Lou[d]*, Kuo-Chuan Ho[b,c]

[a]*Electroanalysis and Bioelectrochemistry Lab, Department of Chemical Engineering and Biotechnology, National Taipei University of Technology, Taipei 10608, Taiwan.*

[b]*Department of Chemical Engineering, National Taiwan University, Taipei 10617, Taiwan.*

[c]*Advanced Research Center for Green Materials Science and Technology, National Taiwan University, Taipei 10617, Taiwan.*

[d]*Chemistry Division, Center for General Education, Chang Gung University, Taoyuan 333, Taiwan.*

ABSTRACT

The defect engineering makes the new concepts and designs to further enhance the electrocatalytic activity of layered structures. In this work, we demonstrated the synthesis of Mn-doped $MoSe_2$ and reported the resultant defective sites. Subsequently, $MnMoSe_2$ was developed as a new type of electrocatalyst for electrochemical biosensors. The formation of defect/distortion and effective immobilization of myoglobin (Mb) were evidently confirmed by using TEM and UV-vis spectroscopy analyses respectively. The result of EIS analysis reveals that the Mn doping not only helps for enzyme immobilization and also enhances the electronic conductivity of layered material. Due to the multiple signal amplification strategies, the proposed Mb immobilized $MnMoSe_2$ (Mb@$MnMoSe_2$) exhibited an ultra-low detection limit (0.004 μM) and higher sensitivity (222.78 μA μM^{-1} cm^{-2}) of H_2O_2. In real sample analysis, the Mb@$MnMoSe_2$ showed a feasible recovery range of H_2O_2 detection in human serum (95.6-102.1%), urine (101.2-102.3%) and rain water (100.7-102.1%) samples. On the other hand, an in-vivo study by using HaCaT ($7.1*10^5$/mL) and RAW 264.7 ($1*10^6$/mL) living cells showed the feasible current responses of 0.096 and 0.085 μA. Finally, the Mn doping gives a new opportunity to fabricate a promising electrocatalyst for H_2O_2 bio-sensing.

Keywords: Molybdenum diselenides, Defect, Manganese, Hydrogen peroxide, Biosensor, In-vitro study, and In-vivo study.

1. INTRODUCTION

Hydrogen peroxide (H_2O_2) has been used in various fields such as pharmaceutical, industrial, fuel cell, and environmental protection[1]. H_2O_2 is naturally generating in human and animals as a short-term indicator of severity. It plays an important role in the activation of immune cells, apoptosis, and vascular remodeling[2]. High level of H_2O_2 production in human system induces the cytotoxic effects leading to cell damage associated with various cell diseases such as alzheimer's, disorder of central nervous system, cardiovascular, and tumor diseases. To avoid

such severe problems, an ultra-low detection of H_2O_2 is considered as an essential process. Various techniques such as mass spectrophotometry[3], chemiluminescence[4], colorimetric[5], fluorescence[6], and electrochemical sensor technique have been developed for H_2O_2 detection[7]. Among them, an electrochemical sensor is considered as most preferable due to easy electrode fabrication, require lower power, low cost, highly sensitive and selective sensing of target analytes[8]. Alternatively, the conventional methods are taking more time to sample preparation, require long time incubation process, number of sample pretreatment steps and require higher power for experiment. The electrochemical sensors excellently convert the electrochemical interaction between active electrode materials and target analyte into the detectable electrical signal[9-13]. Over the past decades, the development of biosensors based on the biomolecules, such as DNA and metalloproteinase/redox enzymes are most widely interested. The metalloproteinase belongs to the heme protein family containing iron core as a prosthetic group which undergoes electrochemical oxidation/reduction reaction over a wide range of potential. One of the most studied metalloproteinase/enzyme is Mb for sensing of H_2O_2. Mb is a cytoplasmic heme protein consists of a single polypeptide chain of amino acids and found in skeletal muscle. Mb contains iron core as a prosthetic group and positioned in between two histidine amino acids. The main physiological function of myoglobin is oxygen storage to enhance the rate of oxygen diffusion[14]. The unique electrochemical properties of Mb make them useful for the biosensing of target molecules. More evidently, *S. Alim et al.* proved a direct electron transfer of Mb based hydrogen peroxide (H_2O_2) sensor with the help of SnO_2 nanofiber-carbon nanotube nanocomposites[15]. *A.T. Ezhil vilian et al.* achieved a higher electron transfer rate of H_2O_2 at Mb-heme-$Fe^{(II)/(III)}$ immobilized Au-Pty-f-MWCNT electrode[16]. However, still the leaching and poor immobilization of enzyme are considered as the major reasons for inhibition of efficient electron transfer between enzyme and electrode. In this regard, various efforts have been made towards biosensor such as (i) use of redox mediator (ii) linkage of bio-

conjugates and (3) amine modification. Although the application of redox mediator and linkage of bio-conjugates successfully prevent the leaching of enzymes from the electrode surface, the fabrication processes make some difficulties by following the multiple and complicated procedures. Therefore, the new and simple approach has been required to enhance both the entrapment of enzyme and direct electron transfer.

Recently, the layered molybdenum di-selenide ($MoSe_2$) is considered as an analogy of graphene, and a new type of layered materials for various applications such as energy storage devices, electrochemical sensors, hydrogen evolution reactions, and dye-sensitized solar cells applications[17-20]. In general, $MoSe_2$ is existing in different crystal phases such as octahedral (1T) and trigonal prismatic (2H). Among these two phases, the 1T phase of $MoSe_2$ exhibits metallic and higher electrocatalytic activity than that of 2H phase[21]. In order to multiple the electrocatalytic activity of $MoSe_2$ layer, various engineering techniques have been developed such as doping with metal or heteroatoms and integrate with the conductive carbon nanomaterials. Especially, the metal doping introducing strain/defect on the basal plane surface and increase the density of active sites. The presence of more active sites facilitates higher electrocatalytic activity and charge transfer conductivity[22]. In addition, the existing of abundant active sites and the defective basal plane can offer the suitable surface for effective entrapment of Mb. For this new approach, Mn was chosen as an efficient dopant and successfully doped into the $MoSe_2$ layer. Recently, *Y. Liu et al.* demonstrated the heterogeneous Mn^{2+} incorporated into a prismatic lattice of $CoSe_2$ and recorded the subtle atomic distortion and concluded the relative enhancement in electrocatalytic activity[23]. Moreover, the doping of Mn can show several features such as (i) the introduction of defects on the basal plane and generate bound excitons (ii) introduce local electronic states that affect electronic localized band structure[24]. More evidently, the Mn dopants bounded between d band structure of Mo and Se through d-d spin coupling leads to the creation of Se vacancies[25]. The presence of Se vacancies activates

the basal plane, through which both electrocatalytic activity and electronic conductivity have been enhanced. Therefore, the defective sites on basal plane of a layered structure due to Mn doping can provide the effective active sites for enzyme immobilization and reduced the distance between the active center and electrode upon enzyme immobilization[26].

In this work, we successfully synthesized Mn-doped $MoSe_2$ with more defect/active sites for effective Mb immobilization. Further, the prepared nanocomposite was developed as an effective electrocatalyst for H_2O_2 sensing. The recorded TEM analysis confirmed the formation of defect/distortion on the basal plane of $MnMoSe_2$ and consequently, UV-vis spectra confirmed the effective entrapment of Mb. The reported electrochemical studies such as cyclic voltammetry and amperometry experiments evidently proved the excellent electrochemical detection of H_2O_2 at Mb@$MnMoSe_2$/GCE, which is comparatively better than that of $MnMoSe_2$/GCE, $MoSe_2$/GCE, and bare GCE. Thus, the proposed sensor exhibited a very low limit of detection and higher sensitivity for H_2O_2 sensing. In addition, both in-vitro and in-vivo real sample analysis was performed by using human serum, urine, and rain water samples. Herein, HaCaT ($7.1*10^5$/mL) and RAW 264.7 ($1*10^6$/mL) living cells were used as the model cell system for in-vivo analysis. Finally, the concentration of H_2O_2 in-vitro and in-vivo studies was clearly reported.

2. EXPERIMENT SECTION

2.1 Materials and reagents

The manganese (II) chloride ($MnCl_2 \cdot 6H_2O$), sodium molybdate dihydrate ($Na_2MoO_4 \cdot 2H_2O$), hydrazine hydrate solution ($N_2H_4 \cdot xH_2O$), selenide powder (Se) and myoglobin (Mb) were purchased from Sigma Aldrich. The electrochemical properties of the prepared samples were tested by using the three-electrode system, whereas the phosphate buffer (pH 7, 0.05 M), glassy carbon electrode, platinum (Pt), and Ag/AgCl were used as the working electrolyte, counter

electrode, and reference electrode respectively. All the chemical reagents were of analytical grade and used without any purification.

2.2. Hydrothermal synthesis of Mn-doped $MoSe_2$

The proposed $MnMoSe_2$ nanosheets were prepared by using a hydrothermal method[27]. In this typical synthesis method, about 0.13 g of $MnCl_2 \cdot 6H_2O$ (0.02M) and 0.16 g of $Na_2MoO_4 \cdot 2H_2O$ were dissolved in 20 ml of water followed by stirring under vigorous conditions for 15 min. After that, about 0.11 g of Se powder was added to the above solution and kept for stirring up to 30 min. To that mixture solution, 10 ml of $N_2H_4 \cdot xH_2O$ was added drop by drop to form the black precipitate. Then the whole solution was kept under magnetic stirring for 2 h. finally, the black precipitate was transferred into the 50 ml Teflon equipped autoclave and kept at 180℃ for 12 h in a hot air oven. After the reaction, the mixture solution was allowed to cool at room temperature. Then the obtained precipitate was washed several times with water/ethanol and dried in 45℃ for overnight.

2.3 Characterization techniques

The surface morphology of as-synthesized samples $MnMoSe_2$ were clearly observed by using the field emission scanning electron microscope (FESEM: ZEISS Sigma 300 microscope). The atomic distortion/defect of samples was recorded by using the transmission electron microscopy (TEM: JEOL 2100F) analysis along with Fast Fourier Transform (FFT) pattern. The crystallographic nature of the $MnMoSe_2$ was reported by using the X-ray diffraction technique (XRD, XPERT-3 diffract meter with Cu K_α radiation (K= 1.54 Å)). The chemical and electronic state of the as-prepared $MnMoSe_2$ was recorded by using X-ray photoelectron spectroscopy (XPS: Thermo scientific multi-lab 2000). The absorption edge of Mb and $MnMoSe_2$ was investigated by using UV spectroscopy (V-770 spectrometer). The Electrochemical impedance spectroscopy (EIS, IM6ex ZAHNER impedance measurement unit) was performed to analyze the interfacial charge transfer resistance (R_{ct}) between the

modified electrode and working electrolyte. Consequently, the electrochemical performances of Mb/$MnMoSe_2$/GCE towards the electrochemical determination of H_2O_2 were studied and compared by using CV (CHI611A analyzer) and amperometric techniques. In all electrochemical studies, the three-electrode electrochemical system was used, where the glassy carbon electrode (GCE) was used as a working electrode, Ag/AgCl/Sat.KCl electrode was used as a reference electrode, and a platinum wire was used as an auxiliary electrode. All of the following electrochemical studies were performed at room temperature.

2.2. Fabrication of Mb immobilized $MnMoSe_2$ nanosheets

Initially, fresh Mb stock solution was prepared by dissolving 5 mg/ml of Mb at pH 7 and stored in -4 C when not in use. For the fabrication process, 1 mg of $MnMoSe_2$ nanosheets was dispersed in 1 mL of ethanol by using ultrasonication for 15 min. Then, about 6 µL $MnMoSe_2$ suspension was drop coated on the surface of GCE and dried at ambient temperature. After drying process, 6 µL Mb solution was dropped on the $MnMoSe_2$ modified electrode and kept for drying at room temperature. Then the Mb immobilized $MnMoSe_2$ nanosheets modified electrodes were rinsed with DD water to remove the weakly bounded materials on GCE. Finally, the Mb/$MnMoSe_2$/GCE was used as an operational electrode in all electrochemical experiments. For the comparison process, the other modified electrodes such as $MoSe_2$/GCE, and $MnMoSe_2$/GCE were fabricated by following the same procedures.

3. RESULTS AND DISCUSSION

3.1. Characterization of $MnMoSe_2$ nanosheets

The structural characterization of $MnMoSe_2$ was performed by using TEM analysis. **Figure. 1 (A-C)** clearly shows the sheet-like structure of $MnMoSe_2$ with more fold on its surface. The presence of defect due to Mn doping can be identified from **Figure. 1D** and then indicated by the yellow dotted circle. **Figure. 1 (E, F)** shows the HRTEM image for the octahedral prismatic atomic arrangement of $MnMoSe_2$ sheet with defective/distortion area (yellow dotted area),

whereas formation of atomic distortion and the defect can evidently be identified. In addition, the HRTEM images show the different domains which confirmed that the $MnMoSe_2$ layer have more active edge sites. In general, the surface energy of edge sites is 2 order higher than that of basal plane.

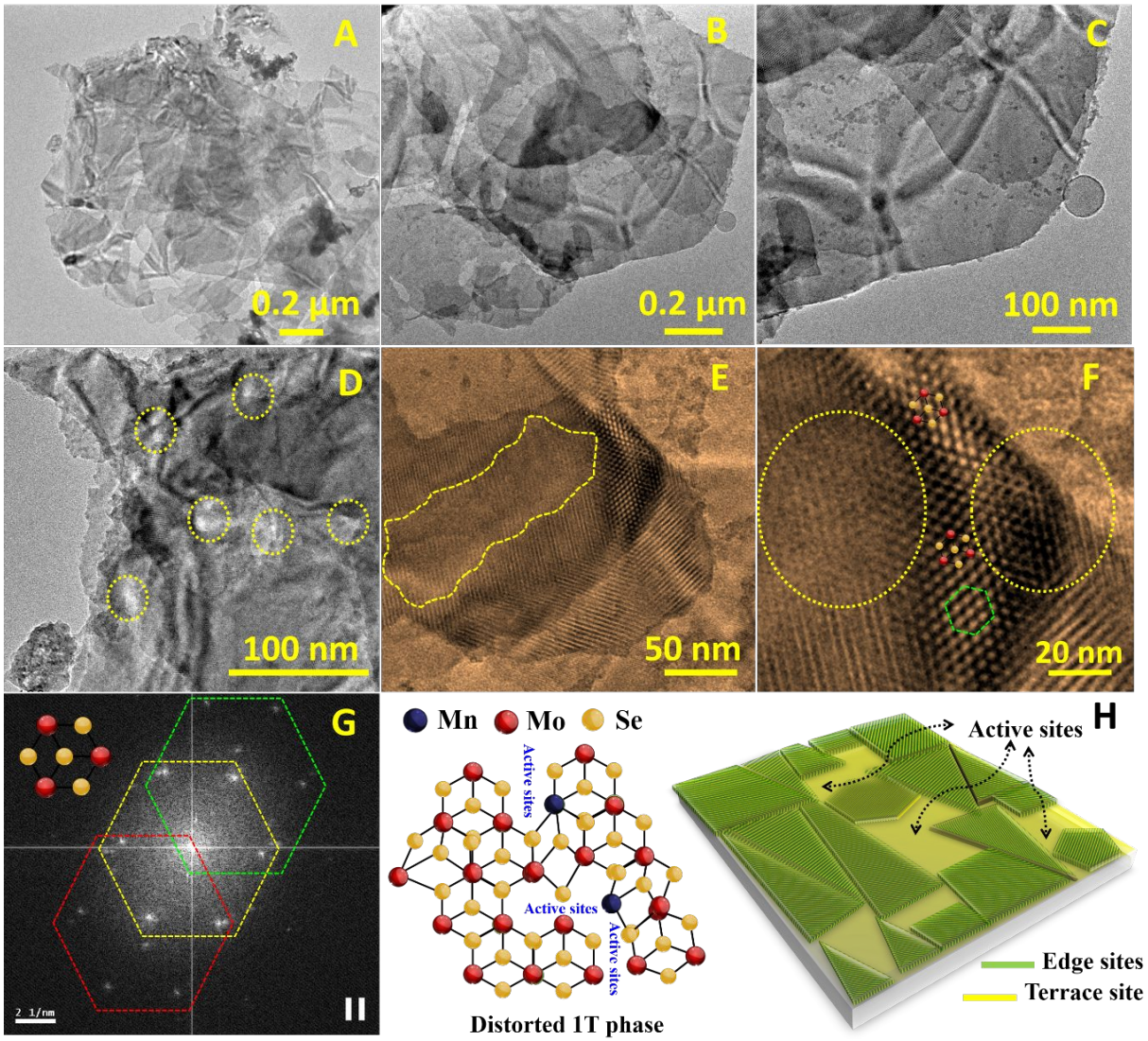

Figure. 1 (A-D) Different magnified TEM images, (E-F) HRTEM, (G) SAED pattern of $MnMoSe_2$ sheet and (H) schematic representation of distorted 1T phase and terrace active sites on $MnMoSe_2$ sheet.

From this TEM analysis, the activation of a basal plane is successfully confirmed by observing the defect/distortion. In addition, the observed terrace sites confirmed the presence of maximally exposed edge sites on the basal plane. The FFT pattern (**Figure. 1G**) shows that octahedral crystalline atomic arrangement of $MnMoSe_2$ with a single set of diffraction spots (6

spots). It confirmed the single phase of prepared $MnMoSe_2$ nanosheets. **Figure. 1H** schematically represents the top view of distorted 1T phase and terrace active sites of $MnMoSe_2$ sheets.

The crystalline nature of $MoSe_2$ and $MnMoSe_2$ was studied by using XRD analysis and reported the corresponding XRD pattern in **Figure. 2**. The XRD pattern of $MoSe_2$ shows the sharp diffraction peak at 12.5 º for (002) crystalline plane. It strongly associated to the XRD pattern of layer $MoSe_2$ as previously reported[28,29]. Meanwhile, the XRD pattern of $MnMoSe_2$ does not show any additional diffraction peaks. It strongly reveals that the Mn dopant is fully dilute and integrate into the crystal lattice of $MoSe_2$, and also the Mn doping does not create any additional phases as an impurity.

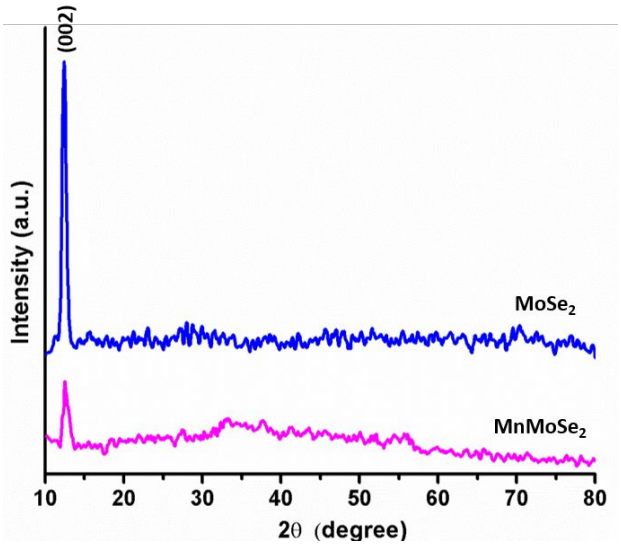

Figure. 2 XRD pattern of $MoSe_2$ and $MnMoSe_2$ sheets

In addition, the elemental composition of $MnMoSe_2$ was estimated by using XPS analysis and reported the resultant wide/high-resolution XPS spectra in **Figure. 3**. In this obtained wide scan spectra (**Figure. 3A**), $MnMoSe_2$ exhibits the peaks for Mn 2p, Mo 3d, O 1s, C 1s, and Se 3d electronic states at 642.96, 530.66, 285.62, 179.55, and 54.51 eV respectively. The resultant peak for C 1s and O 1s are associated to surface reactivity to various hydrocarbon contaminants

in an air atmosphere. The high-resolution XPS spectra of Mn 2P (**Figure. 3B**) shows the Mn $2p_{3/2}$ and Mn $2p_{1/2}$ peaks at the binding energy of 643.36 and 655.53 eV respectively, which contains the valence states of Mn^{3+} and Mn^{4+}. It represents the mixed valence state of Mn in the proposed sample. The high-resolution spectra of Mo 3d **(Figure. 3C)** shows binding energy of 235.36 and 237.83 eV for corresponding doublet Mo^{6+} $3d_{5/2}$ and Mo^{6+} $3d_{3/2}$ levels respectively. And also, it shows two more peaks at 232.41 and 227.98 eV for Mo^{4+} $3d_{5/2}$ and Mo^{4+} $3d_{3/2}$ levels respectively. **Figure. 3D** shows the XPS spectra of Se 3d, which shows the three characteristic peaks at 50.31, 54.17 and 57.12 eV for Se $3d_{5/2}$ and Se $3d_{3/2}$ states respectively. From this XPS result, we estimated that the prepared $MnMoSe_2$ sample formed successfully and the surface region contains only the major constituents such as Mn, Mo and Se elements.

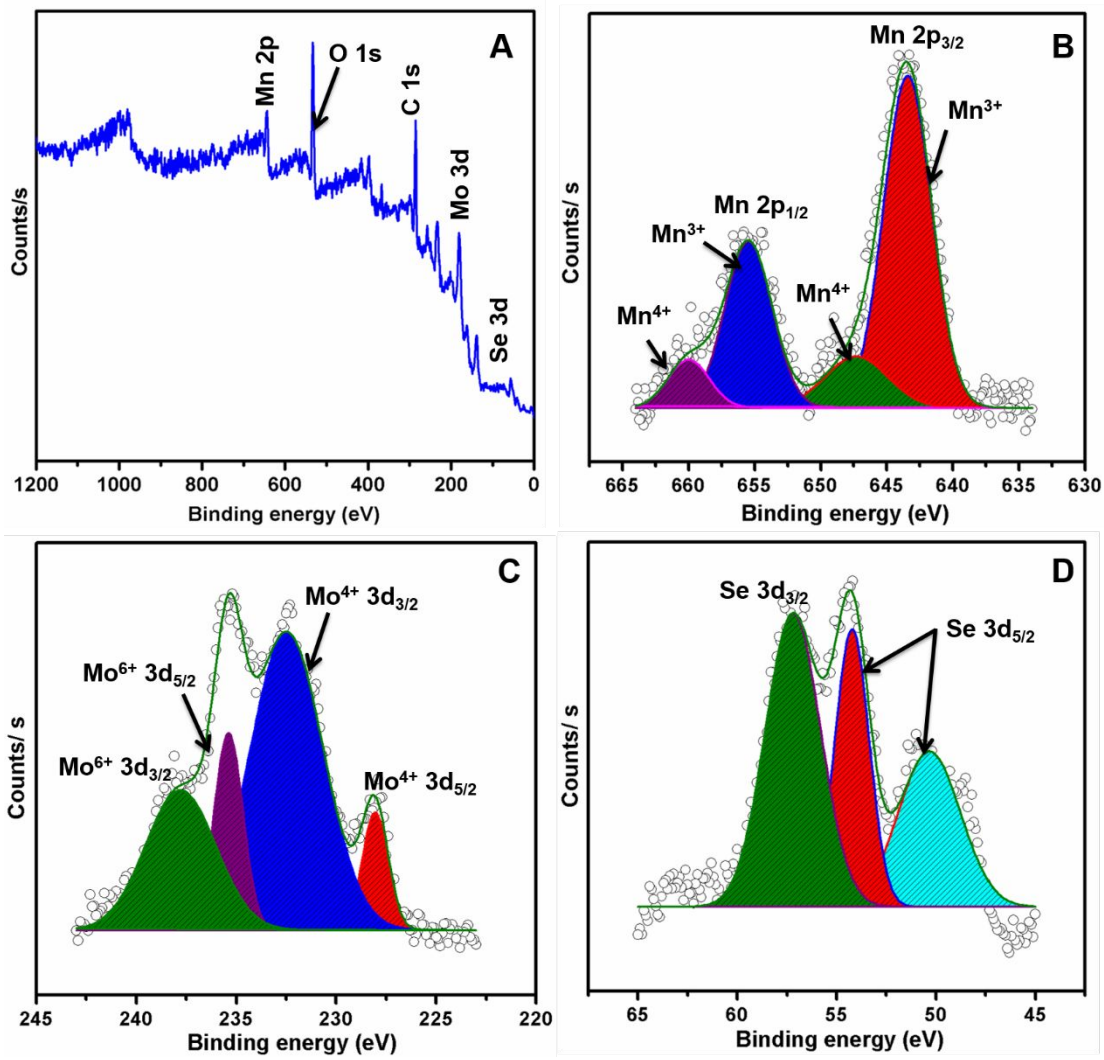

Figure. 3 (A) Wide scan XPS spectra, (B-D) high resolution XPS spectra of $MnMoSe_2$ sheets.

UV-vis spectroscopy is a promising technique to identify the structural profile of Mb in the prepared composite. **Figure. 4** shows UV-vis spectra of Mb@$MnMoSe_2$ composite with the sharp characteristic bands such as Soret band, Q band, and CT1 band at 409.8, 502.8 and 633.3 nm respectively, which are associated to the His93 residue (high-spin heme with histidine) and H_2O molecular bond at 5^{th} and 6^{th} coordination position of Fe atom in Mb. Thus, the resultant UV-vis spectra evidently confirmed the immobilization of Mb with $MnMoSe_2$. Meanwhile, the UV-vis signal of $MnMoSe_2$ is significantly quenched, which is related to its metallic nature (1T octahedral coordination).

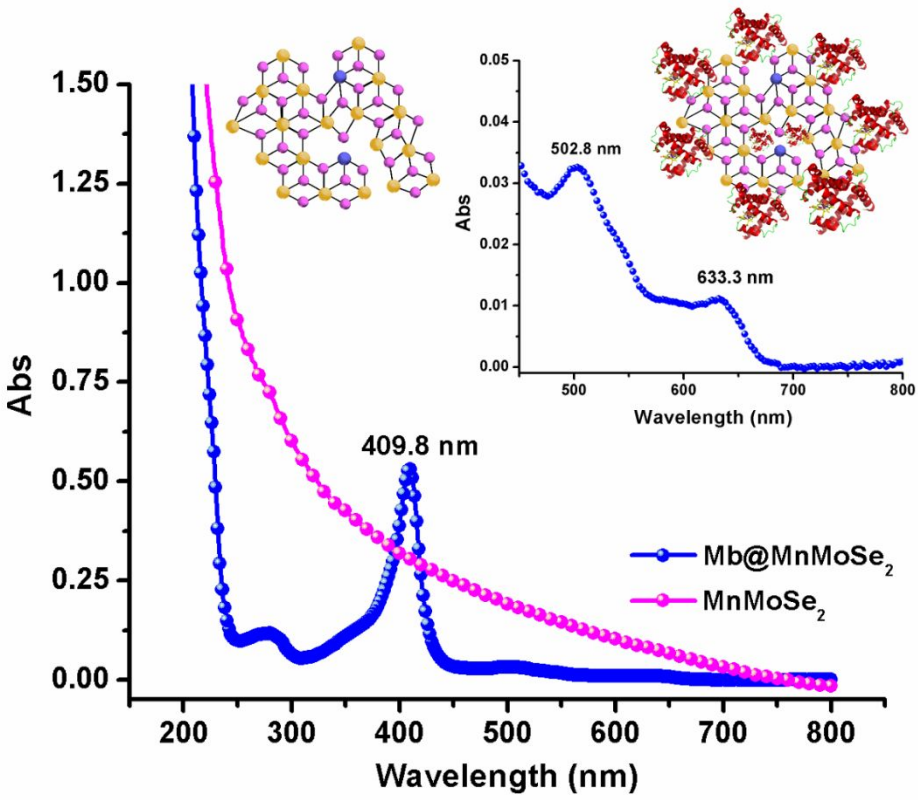

Figure. 4 UV-visible spectra of $MnMoSe_2$, Mb@$MnMoSe_2$ and (inset) maximized UV spectra of $MnMoSe_2$.

4. Electrochemical properties of Mb@$MnMoSe_2$ modified electrode

The successful immobilization of Mb on $MnMoSe_2$ and the resultant electrochemical properties were studied by using the EIS technique. From this technique, the charge transfer resistance (R_{ct}) at an interface between the electrolyte and different electrodes (Bare GCE, $MoSe_2$/GCE, $MnMoSe_2$/GCE, Mb/GCE, and Mb@$MnMoSe_2$/GCE) were detected. In general, the R_{ct} is inversely proportional to fast electron transfer at the electrode/electrolyte interface. Thus, the EIS experiment was performed for bare GCE, $MoSe_2$/GCE, $MnMoSe_2$/GCE, Mb/GCE, and Mb@$MnMoSe_2$/GCE in ferricyanide redox system at a fixed frequency range ($1*10^{-1}$ Hz to $1*10^{2}$ KHz) whereas the applied potential is constant of about 0.01 V. The resultant Nyquist plot is shown in **Figure. 5(A, B)**, from which the R_{ct} of bare GCE, $MoSe_2$/GCE, $MnMoSe_2$/GCE, Mb/GCE, and Mb@$MnMoSe_2$/GCE were detected to be 174.3, 30.3, 12.1, 330.2, and 184.4 Ω respectively. It clearly demonstrated in the bar diagram as shown in **Figure. 5C**. The resultant lower R_{ct} gives strong evidence that Mn doping significantly enhances the electronic conductivity of $MoSe_2$. Meanwhile, the increasing R_{ct} at Mb@$MnMoSe_2$/GCE reveals the successful immobilization of Mb on $MnMoSe_2$/GCE. Herein, the Mb is only functioning as an effective catalyst to induce the electrochemical reaction between target analyte and electrode.

Figure. 5B (inset) shows the corresponding Randle's circuit, which reveals that the electrochemical properties at the electrode/electrolyte interface is ascribed from the various dynamics such as charge transfer resistance (R_{ct}), solution resistance (R_s), Warburg impedance (Z_w), and double layer capacitance (C_{dl}). Finally, the successful immobilization of Mb and Mn doping can effectively enhance the electrochemical sensing of H_2O_2.

4.1. Electrochemical sensing of H_2O_2 at Mb@$MnMoSe_2$/GCE

The electrochemical sensing of H_2O_2 was studied at Mb@$MnMoSe_2$/GCE and compared with other modified electrodes of $MnMoSe_2$/GCE, $MoSe_2$/GCE, and bare GCE. For this sensing analysis, the CV technique was performed for different modified electrodes in N_2 purged

electrolyte with the presence of H_2O_2 (0.196 mM), whereas the scan rate was fixed to 50 mV s^{-1}. The obtained CV curves **(Figure. 5D)** show that Mb/$MnMoSe_2$/GCE exhibited an enhanced current response (204.9 µA) for the reduction of H_2O_2. Meanwhile, the $MnMoSe_2$/GCE, $MoSe_2$/GCE, and bare GCE exhibited the current response of about 145.9, 82.94, and 11.34 µA respectively. It clearly reveals that Mb@$MnMoSe_2$/GCE showed 0.4, 1.4 and 17.06 fold higher current response than obtained at $MnMoSe_2$/GCE, $MoSe_2$/GCE, and bare GCE respectively, which clearly displays in the bar diagram **(Figure. 5E)**.

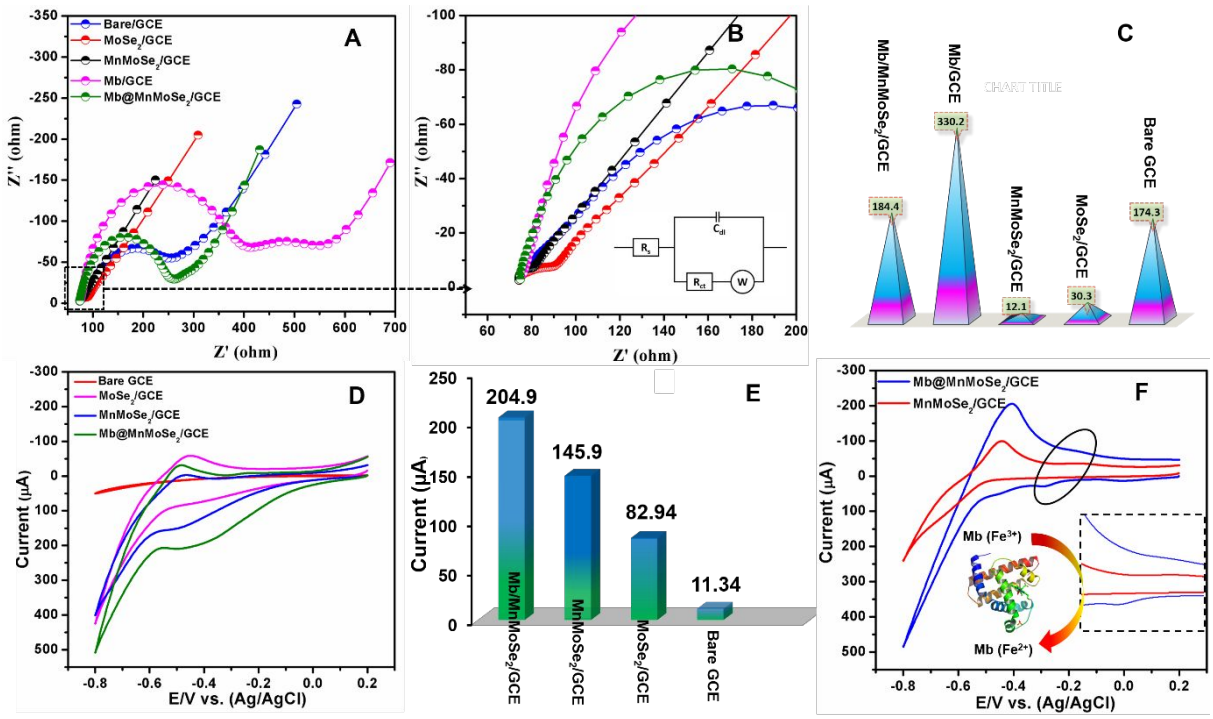

Figure.5 (A, B) Nyquist plot of different modified electrodes, (C) corresponding bar diagram between different electrodes vs. corresponding R_{ct} value, (D) CV curve of different modified electrodes for electrochemical sensing of H_2O_2, (E) corresponding bar diagram among different modified electrodes vs. reduction current response. (F) CV curves for background current responses of Mb@$MnMoSe_2$/GCE and $MnMoSe_2$/GCE.

The obtained results indicate that bioactive electrocatalyst Mb is greatly supporting to effective electrochemical reduction of H_2O_2 at Mb@$MnMoSe_2$/GCE. In the case of $MnMoSe_2$, the Mn doping promotes not only the electronic conductivity but also enhances the electrocatalytic activity of $MoSe_2$ by creating the atomic lattice distortion and defect. Thus, $MnMoSe_2$/GCE showed an improved electrochemical reduction response of H_2O_2 than that of $MoSe_2$/GCE.

Herein, the presence of atomic defects on $MnMoSe_2$ also provides abundant active sites and a suitable surface for effective immobilization of Mb. The effective immobilization of Mb on $MnMoSe_2$ was evidently confirmed by observing the reduction and oxidation peaks at -0.3 and 0.1 V respectively (**Figure. 5F**). It indicates that the Fe^{3+} active sites in the center of Mb electrochemically transformed into Fe^{2+}. The electrochemical reaction mechanism between H_2O_2 and Mb at the modified electrode can be denoted as below,

Mb *heme* (Fe^{3+}) + e → Mb *heme* (Fe^{2+})

2Mb *heme* (Fe^{2+}) + $2H^+$ + H_2O_2 → 2Mb *heme* (Fe^{3+}) + $2H_2O$

The observed electrochemical reduction of H_2O_2 at the proposed Mb@$MnMoSe_2$/GCE is clearly represented in **Scheme 1**.

Scheme 1. Schematic illustration for electrochemical reduction of H_2O_2 at Mb@$MnMoSe_2$/GCE.

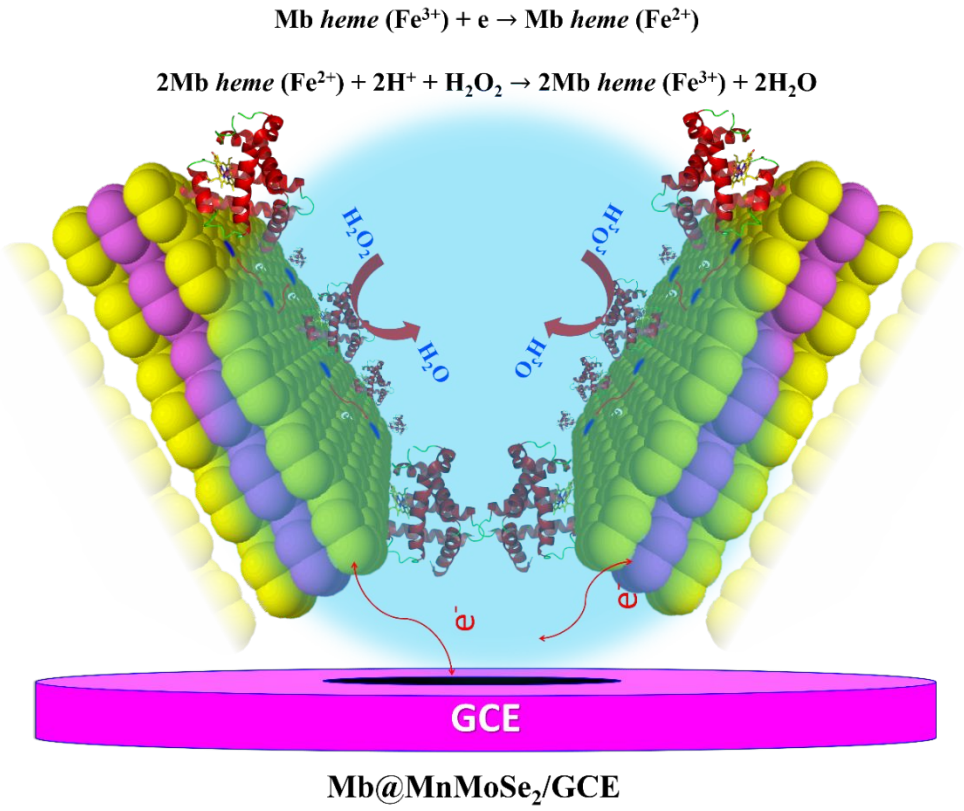

The electrochemical reduction of H_2O_2 was studied at Mb@$MnMoSe_2$/GCE by varying the scan rate from 10 to 50 mV s^{-1}, whereas the concentration of H_2O_2 is constant of about 0.196

mM in N_2 purged electrolyte. The resultant CV curve **(Figure. 6A)** shows the linearly increasing reduction peak for increasing the scan rate. The linear relationship between the reduction current response and the scan rate is demonstrated in the calibration plot **(Figure. 6B)**. From this plot, the linear regression equation and correlation coefficient were detected to be I_{pc} (μA) = 4.284 (v (mV s^{-1})) + 55.16 and R^2 = 0.986 respectively. It indicates that the electrochemical reduction of H_2O_2 at Mb@$MnMoSe_2$/GCE followed a surface controlled process. The obtained correlation coefficient is nearly equal to 1, which implies that the proposed modified electrode suffers less kinetic limitation only. It is so favorable for efficient electrochemical detection of H_2O_2.

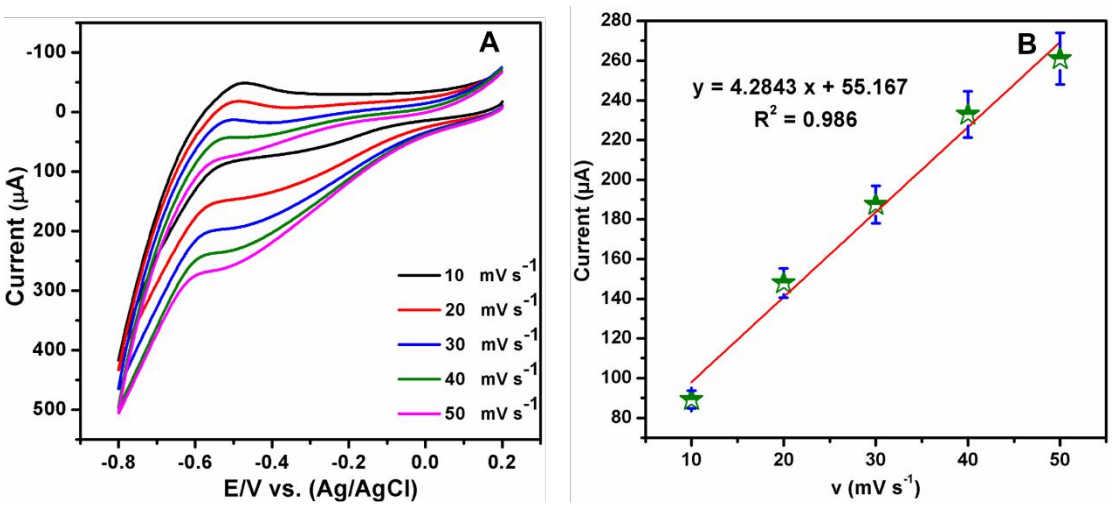

Figure 6. (A) CV curve for different scan rate at Mb@$MnMoSe_2$/GCE with presence of H_2O_2 (0.196 mM) and (B) corresponding linear calibration curve for scan rate vs. reduction current response.

The quantitative detection of H_2O_2 at Mb@$MnMoSe_2$/GCE was analyzed by using the amperometric i-t technique. For this experiment, the optimization study was carried out to find out a suitable electrode potential, whereas the applied potential was varied in order of -0.35, -0.40, -0.45, and -0.50 V. For different applied potential, the concentration of H_2O_2 was stepwise increased and recorded the corresponding amperometric i-t responses as shown in **Figure. 7A.** From the amperometric i-t curves, the stable and linear stepwise increment of current response has been observed for -0.45 V. In case of other applied potentials (-0.35, -0.40, and -0.50 V), the background current and H_2O_2 current responses comparatively lower and sluggish. It clearly

displays in **Figure. 7B,** with detected current signal time for different potentials. Among these applied potentials, the current signal time is comparatively lower for -0.45 V to be 1.5 s. Meanwhile, the signal time was detected for -0.35, -0.40 and -0.50 V to be 2.1, 3.5, and 3.5 s respectively. Thus, we concluded that the -0.45 V is as an optimized electrode potential for electrochemical reduction of H_2O_2.

Figure. 7C shows the amperometric i-t curve for linear addition of H_2O_2 concentration from 0.09 to 60 µM, whereas the optimized -0.45 V was fixed as an electrode potential and electrode rotation speed was fixed to be 1200 rpm. The resultant amperometric curve shows the linear and stepwise increasing of current for the stepwise addition of H_2O_2. The corresponding linear calibration plot for concentration vs. oxidation current is demonstrated in (**Figure. 7D**) with linear calibration equation and correlation coefficient of I_{pc} (µA) = 3.734 (µM) + 18.74 and R^2 = 0.9981 respectively. The resultant correlation coefficient indicates that the proposed Mb@$MnMoSe_2$/GCE exhibited an excellent linear current response for the addition of H_2O_2.

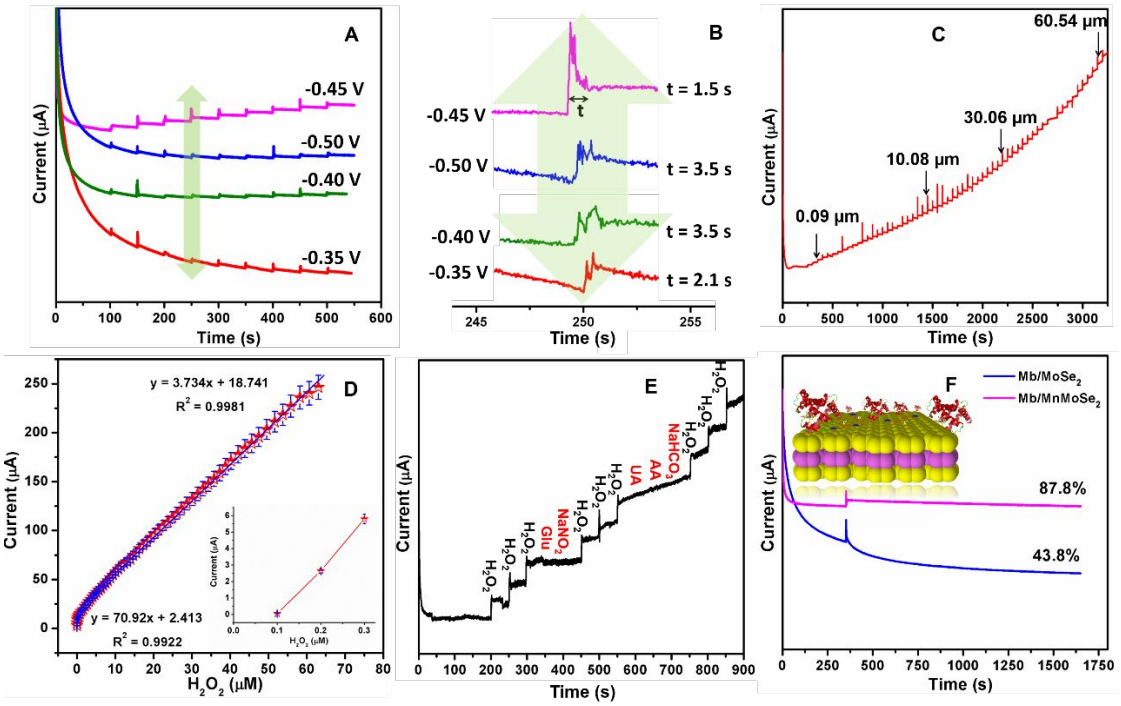

Figure 7. (A) Amperometric i-t curve for different applied potentials, (B) corresponding maximized peak response, (C) amperometric i-t curve for addition of different concentrations of H_2O_2, (D) corresponding linear calibration curve (inset: linear calibration plot for lower concentration of H_2O_2),

and amperometric i-t curve for (E) interference and (F) stability studies (inset: schematic illustration of Mb@$MnMoSe_2$).

From the detected slope value, the sensitivity and detection limit for the reduction of H_2O_2 at Mb@$MnMoSe_2$/GCE were calculated by using equation (1),

$$LOD = 3\sigma/S \quad [1]$$

where the σ is denoted as the standard deviation and S is represented as the slope of the linear plot. By substituting the slope of the linear regression equation, the detection limit was calculated to be 0.004 μM. In addition, the sensitivity (slope/active surface area) for the detection of H_2O_2 at Mb@$MnMoSe_2$/GCE was detected to be 222.78 μA μM^{-1} cm^{-2}. Consequently, the obtained detection limit and sensitivity were compared with previously reported H_2O_2 sensor and demonstrated in **Table 1**.

Table 1. comparison of electrochemical sensing at different modified electrodes

Electrode	Techniques	Linear range (μM)	LOD (μM)	Sensitivity ($\mu A \mu M^{-1} cm^{-2}$)	Reference
Mb/S-MCF/GCE	Amperometric i-t	1–80	0.18	2.2	8
g-CNTs/PBMCs/GCE	Amperometric i-t	0.025–1598	0.013	1.328	32
Mb/GO@MoS_2	Amperometric i-t	20-100	0.02	-	7
GC-2	fluorescence	0-120	0.21	-	6
MoS_2@$MgFe_2O_4$	colorimetric	25-300	1	-	5
PLL/f-MWCNT	Amperometric i-t	1-3600	0.008	392	33
f-MWCNT-P-L-His-ZnO	Amperometric i-t	4-18,000	0.01	35.71	34
HPLC/ED	HPLC	7.4-15,000	0.6	-	35
HPLC/martial soil	HPLC	0.2-100	0.1	-	36
Mb@$MnMoSe_2$/**GCE**	**Amperometric i-t**	**0.09-60**	**0.004**	**222.78**	**This work**

From this comparison table, the proposed electrochemical sensor comparatively exhibited the better quantitative result towards the H_2O_2 detection. Thus, the Mb@$MnMoSe_2$/GCE has identified a promising electrode for H_2O_2 sensing.

The selectivity study was performed for the proposed sensor Mb@$MnMoSe_2$/GCE by using the amperometric i-t technique with similar working conditions as mentioned above. The amperometric i-t curve for the addition of H_2O_2 (**Figure. 7E)** and 100-fold higher concentration of potential interfering compounds (Glucose (Glu), $NaNO_2$, uric acid (UA), ascorbic acid (AA), and $NaHCO_3$). From this amperometric i-t curve, the sharp and immediate current response was observed for the addition of H_2O_2 only, whereas the addition of interfering compounds does not show any peak responses. It implies that the proposed sensor exhibited the higher selective sensing towards H_2O_2 reduction. Furthermore, the stability of the Mb@$MnMoSe_2$/GCE was analyzed and compared with $MnMoSe_2$/GCE as shown in **Figure. 7F.** In this experiment, the Mb@$MnMoSe_2$/GCE exhibited the 87.8% of its initial reduction current response of H_2O_2 (0.15 μM) after 1600 s. At the same time, Mb/$MoSe_2$/GCE showed only 43.8% of its initial reduction current response. It clearly indicates that the Mn doping is offering abundant active sites and distortion/defect on the basal plane of $MoSe_2$, which is most favorable for effective immobilization of Mb. Hence, the Mb is strongly entrapped on Mn-doped $MoSe_2$ and relatively enhanced the sensing of H_2O_2.

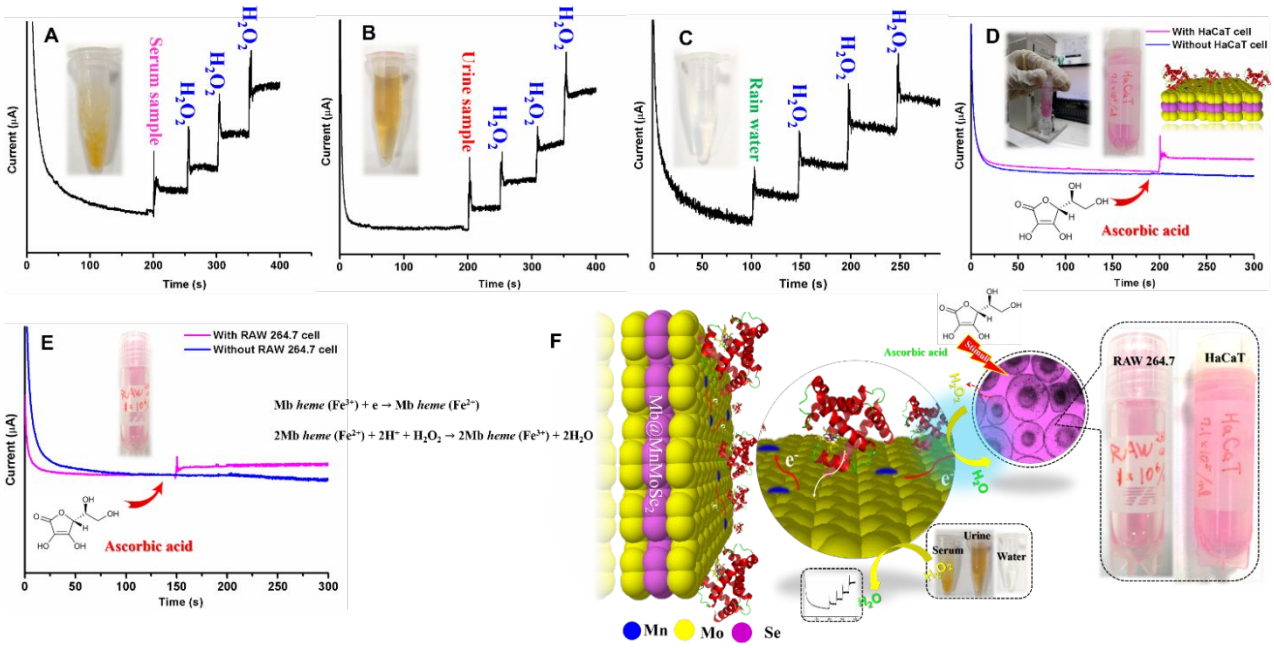

Figure 8 Amperometric i-t curve for real sample analysis by using (A) human serum sample, (B) human urine sample, (C) Rain water (D) HaCaT living cell (E) RAW 264.7 living cells, and (F) schematic illustration for real sample analysis.

4.7. Real-time in vitro sensing of H_2O_2 from human serum, urine and rain water samples

The feasible practicability of the prepared sensor was studied by using the real sample analysis. For this, the amperometric i-t technique was performed in an optimized working condition as mentioned in the above experiments. By following the standard titration method, the human serum, urine, water samples were diluted in 0.1 M PBS solution for three times, and then directly added into the working solution. Consequently, the known concentration of H_2O_2 spiked serum, urine, water samples were added as shown in **Figure. 8 (A-C).** The standard concentration of H_2O_2 in un-spiked and spiked samples were detected by using the standard regression linear plot (**Figure. 7D**) and then the obtained results were tabulated as shown in **Table 2**.

As the results, the recovery ratio was detected in the range of 95.6-102.1%, 101.2-102.3% and 100.7-102.1 % for H_2O_2 spiked serum, urine and rain water samples respectively. Finally, the obtained recovery ratio reveals the effective sensing performance of Mb@$MnMoSe_2$ towards H_2O_2 in human serum, urine sample and rain water samples.

Table 2: Results of real sample analysis of H_2O_2 in human serum, urine and rain water samples.

Sample	Found (µM)	Added (µM)	After added (µM)	RSD (%)	Recovery (%)
Serum	0.233	0	0.233	2.7	-
	0.233	0.2	0.414	2.4	95.6
	0.233	0.4	0.642	2.0	101.4
	0.233	0.6	0.851	2.2	102.1
Urine	0.175	0	0.175	1.8	-
	0.175	0.2	0.381	1.4	101.6
	0.175	0.4	0.582	2.3	101.2
	0.175	0.6	0.793	1.9	102.3
Rain Water	0.31	0	0.31	2.5	-
	0.31	0.2	0.52	2.1	101.9
	0.31	0.4	0.725	2.3	102.1
	0.31	0.6	0.917	2.8	100.7

4.7. Real-time in vivo sensing of H_2O_2 from living cells (HaCaT and RAW 264.7 living cells)

Hydrogen peroxide (H_2O_2) is naturally generating in human and animals as a short-term indicator of severity (ex., a biomarker of cancer). Hence, the ultra-low determination of H_2O_2 concentration related to the normal function of living organisms is so much essential to understand the functional process of living organisms. Therefore, HaCaT ($7.1*10^5$/mL) and RAW 264.7 ($1*10^6$/mL) living cells were chosen as the model cells and AA was used as a stimulant to estimate the sensing behavior of Mb@$MnMoSe_2$/GCE. Before the experiment, the HaCaT and RAW 264.7 were removed from the cell culture and washed two times by using 0.1 M PBS electrolyte. Then, the amperometric i-t technique was performed by adding the 5 µM of AA stimulant in PBS with/without living cells and observed the amperometric i-t curve as shown in **Figure. 8(D, E)**. In this curve, a suddenly increasing current response was observed for the addition of AA in PBS with living cells. Meanwhile, only a background current was observed with no any current response in PBS without living cells. From this results, we can understand that AA successfully stimulated the H_2O_2 endogenously from the living cells and sensitively detected by the proposed Mb@$MnMoSe_2$/GCE sensor. The maximum current

change was detected for HaCaT living cell to be 0.096 μA for equivalent H_2O_2 concentration of 0.12 μM (linear regression plot). At the same time, the current response for RAW 264.7 was obtained to be 0.085 μA corresponding to H_2O_2 (0.10 μM) as calculated in linear regression plot (**Figure. 7D (inset)**). The obtained results are strongly associated with the previous literature[30,31]. Finally, the proposed sensor is found as the potential electrocatalyst to determine the H_2O_2 released from the living cells, it is schematically represented in **Fig. 8F**.

5. CONCLUSION

In summary, we scrutinized that the presence of defect/distortion in the basal plane of $MnMoSe_2$ offers a suitable surface for effective immobilization of Mb. All characterization techniques including TEM, SAED, XRD, XPS and UV-vis analyses confirmed the formation of $MnMoSe_2$ nanosheets and successful immobilization of Mb. In addition, EIS, CV and amperometric i-t techniques scrutinized the improved electrocatalytic and electronic conductivity of the proposed sensor. As a results, the Mb entrapped $MnMoSe_2$/GCE layer exhibited a higher electrochemical reduction response towards the H_2O_2 sensing, which is comparatively better than other $MnMoSe_2$/GCE, $MoSe_2$/GCE, and bare GCE. Furthermore, the proposed enzyme immobilized electrocatalysts showed very low detection limit (0.004 μM) and higher sensitivity (222.78 $\mu A\ \mu M^{-1}\ cm^{-2}$) towards H_2O_2 sensing. Due to the feasible electrocatalytic activity, the Mb@$MnMoSe_2$/GCE was further applied to real-time sensing of H_2O_2 by using in-vitro and in-vivo studies. In this real-time studies, the electrochemical response of H_2O_2 was successfully recorded by using the model real samples such as human serum, urine, rain water samples, HaCaT ($7.1*10^5$/mL), and RAW 264.7 ($1*10^6$/mL) living cells. From these experimental studies, we concluded that Mn doping into $MoSe_2$ facilitates higher electrocatalytic activity and effective immobilization of enzyme for enhanced electrochemical sensing of H_2O_2.

ACKNOWLEDGEMENTS

Financial supports of this work by the Ministry of Science and Technology, Taiwan (MOST 107-2113-M-027-005-MY3 to SMC) is gratefully acknowledged. This work was partially supported by the "Advanced Research Center for Green Materials Science and Technology" from The Featured Area Research Center Program within the framework of the Higher Education Sprout Project by the Ministry of Education (107L9006) and the Ministry of Science and Technology in Taiwan (MOST 105-2221-E-002-229-MY3, 107-2811-E-002-559, and 107-3017-F-002-001).

AUTHOR INFORMATION

Corresponding Authors

*E-mail: smchen78@ms15.hinet.(S.M.Chen)

*E-mail: blou@mail.cgu.edu.tw (Bih-Show Lou)

NOTES

The authors declare no competing financial interest

REFERENCES

1. Qi, L., Hu, Q., Kang, Q., Yu, L. Fabrication of Liquid-Crystal-Based Optical Sensing Platform for Detection of Hydrogen Peroxide and Blood Glucose. *Anal. Chem.* **2018**, 90, 11607-11613.
2. Ren, Q.Q., Wu, J., Zhang, W.C., Wang, C., Qin, X., Liu, G.C., Li, Z.X., Yu, Y. Real-time in vitro Detection of Cellular H_2O_2 under Camptothecin Stress Using Horseradish Peroxidase, Ionic Liquid, and Carbon Nanotube-Modified Carbon Fiber Ultramicroelectrode. *Sens.Actuator B-Chem*. **2017**, 245, 615-621.
3. Cochemé, H.M., Quin, C., McQuaker, S.J., Cabreiro, F., Logan, A., Prime, T.A., Abakumova, I., Patel, J. V., Fearnley, I.M., James, A.M., Porteous, C.M., Smith, R.A.J., Saeed, S., Carré, J.E., Singer, M., Gems, D., Hartley, R.C., Partridge, L., Murphy, M.P. Measurement of H_2O_2 within Living Drosophila during Aging Using a Ratiometric

Mass Spectrometry Probe Targeted to the Mitochondrial Matrix. *Cell Metab.* **2011**, 13, 340–350.

4. Nakano, K., Honda, T., Yamasaki, K., Tanaka, Y., Taniguchi, K., Ishimatsu, R., Imato, T. Carbon Quantum Dots as Fluorescent Component in Peroxyoxalate Chemiluminescence for Hydrogen Peroxide Determination. *Bull. Chem. Soc. Jpn.* **2018**, 91, 1128–1130.
5. Zhang, Y., Zhou, Z., Wen, F., Tan, J., Peng, T., Luo, B., Wang, H., Yin, S. A Flower-like MoS_2-decorated $MgFe_2O_4$ Nanocomposite: Mimicking Peroxidase and Colorimetric Detection of H_2O_2 and Glucose. *Sens.Actuator B-Chem.* **2018**, 275, 155–162.
6. Li, N., Huang, J., Wang, Q., Gu, Y., Wang, P. A Reaction Based One- and two-photon Fluorescent Probe for Selective Imaging H_2O_2 in Living Cells and Tissues. *Sens.Actuator B-Chem.* **2018**, 254, 411–416.
7. Yoon, J., Lee, T., Bapurao, B., Jo, J., Oh, B.K., Choi, J.W. Electrochemical H_2O_2 Biosensor Composed of Myoglobin on MoS_2 Nanoparticle-Graphene Oxide Hybrid Structure. *Biosens. Bioelectron.* **2017**, 93, 14–20.
8. Jahanbakhshi, M. Myoglobin Immobilized on Mesoporous Carbon Foam in a Hydrogel (selep) Dispersant for Voltammetric Sensing of Hydrogen Peroxide. *Microchim. Acta* **2018**, 185, 233-247.
9. Khodadadi, A., Mirzaei, E.F., Maleh, H.K., Abbaspourrad, A., Agarwal, S., Gupta V.K. A New Epirubicin Biosensor Based on Amplifying DNA Interactions with Polypyrrole and Nitrogen-Doped Reduced Graphene: Experimental and Docking Theoretical Investigations. *Sens.Actuator B-Chem*. **2019**, 284, 568-574.
10. F.T., Javazmi, M.S., Nooshabadi, Maleh, H.K. Analysis of Glutathione in the Presence of Acetaminophen and Tyrosine via an Amplified Electrode with MgO/SWCNTs as a Sensor in the Hemolyzed Erythrocyte. *Talanta* **2018**, 176, 208–213.
11. Tabari, S.A.R.A., Khalilzadeh, M.A., Maleh, H.K., Zareyee, D. An Amplified Platform Nanostructure Sensor for the Analysis of Epirubicin in the Presence of Topotecan as Two Important Chemotherapy Drugs for Breast Cancer Therapy. *New J. Chem.* **2018**, 42, 3828.
12. Javazmi, F.T., Nooshabadi M.S., Maleh H.K. Gold Nanoparticles and Reduced Graphene Oxide-amplified Label-free DNA Biosensor for Dasatinib Detection. *New J. Chem.* **2018**, 42,16378.

13. Emamian, R., Ebrahimi, M., Maleh, H.K. Electrochemical Platform Based on Synergic Effect of Fe_3O_4/SWCNTs and 1-ethyl-3-methyl Imidazolium Chloride as Sensor for Determination of Xanthine and Theophylline in Food Samples. *J. Electrochem. Soc.* **2018**, 165, 762-766.
14. Ordway, G.A. Myoglobin: An Essential Hemoprotein in Striated Muscle. *J. Exp. Biol.* **2004**, 207, 3441–3446.
15. Alim, S., Kafi, A.K.M., Jose, R., Yusoff, M.M., Vejayan, J. Enhanced Direct Electron Transfer of Redox Protein Based on Multiporous SnO_2 Nanofiber-Carbon Nanotube Nanocomposite and its Application in Biosensing. *Int. J. Biol. Macromol.* **2018**, 114, 1071–1076.
16. Vilian, A.T.E., Veeramani, V., Chen, S.M., Madhu, R., Kwak, C.H., Huh, Y.S., Han, Y.K. Immobilization of Myoglobin on Au Nanoparticle-Decorated Carbon Nanotube/Polytyramine Composite as a Mediator-free H_2O_2 and Nitrite Biosensor. *Sci. Rep.* **2015**, 5, 1–10.
17. Eftekhari, A. Molybdenum Diselenide ($MoSe_2$) for Energy Storage, Catalysis, and Optoelectronics. *Appl. Mater. Today* **2017**, 8, 1–17.
18. Selvarani, K., Prabhakaran, A., Arumugam, P., Berchmans, S., Nayak, P. 2D $MoSe_2$ Sheets Embedded Over a High Surface Graphene Hybrid for the Amperometric Detection of NADH. *Microchim. Acta* **2018**, 185, 411-419.
19. Gao, D., Xia, B., Wang, Y., Xiao, W., Xi, P., Xue, D., Ding, J. Dual-Native Vacancy Activated Basal Plane and Conductivity of MoSe2 with High-Efficiency Hydrogen Evolution Reaction. *Small* **2018** 14, 1-8.
20. Yuan, X., Zhou, B., Zhang, X., Li, Y., Liu L. Hierarchical $MoSe_2$ Nanoflowers Used as Highly Efficient Electrode for Dye-Sensitized Solar Cells. *Electrochim. Acta* **2018**, 283, 1163-1169.
21. Yu, Y., Nam, G.H., He, Q., Wu, X.J., Zhang, K., Yang, Z., Chen, J., Ma, Q., Zhao, M., Liu, Z., Ran, F.R., Wang, X., Li, H., Huang, X., Li, B., Xiong, Q., Zhang, Q., Liu, Z., Gu, L., Du, Y., Huang, W., Zhang, H. High Phase-purity 1T′-MoS_2- and 1T′-$MoSe_2$-layered crystals. *Nat. Chem.* **2018**, 10, 638-643.
22. Chen, Y., Yang, K., Jiang, B., Li, J., Zeng, M., Fu, L. Emerging Two-dimensional Nanomaterials for Electrochemical Hydrogen Evolution. *J. Mater. Chem. A* **2017**, 5, 8187-8208.

23. Liu Y., Pan B., Hua X., Xie Y., Xiao C., Zhou T., Huang P., Guo Z. Heterogeneous Spin States in Ultrathin Nanosheets Induce Subtle Lattice Distortion to Trigger Efficient Hydrogen Evolution. *J. Am. Chem. Soc.* **2016,** *138*, 5087-5092.
24. Zhang, K., Feng, S., Wang, J., Azcatl, A., Lu, N., Addou, R., Wang, N., Zhou, C., Lerach, J., Bojan, V., Kim, M.J., Chen, L.Q., Wallace, R.M., Terrones, M., Zhu, J., Robinson, J.A. Manganese Doping of Monolayer MoS_2: The Substrate Is Critical. *Nano Lett.* **2015**, 15, 6586–6591.
25. Zhao, X., Dai, X., Xia, C., Wang, T., Peng, Y. Electronic and Magnetic Properties of Mn-Doped Monolayer WS_2. *Solid State Commun.* **2015**, 215, 1-4.
26. Zhou, W.Y., Li, S.S., Xiao, X.Y., Chen, S.H., Liu, J.H., Huang, X.J. Defect- and Phase-Engineering of Mn-mediated MoS_2 Nanosheets for Ultrahigh Electrochemical Sensing of Heavy Metal Ions: Chemical Interaction-Driven in Situ Catalytic Redox Reactions. *Chem. Commun.* **2018**, 54, 9329-9332.
27. Sakthivel, M., Sukanya, R., Chen, S.M., Ho, K.C. Synthesis and Characterization of Samarium-Substituted Molybdenum Diselenide and Its Graphene Oxide Nanohybrid for Enhancing the Selective Sensing of Chloramphenicol in a Milk Sample. *ACS Appl. Mater. Interfaces* **2018**, 10, 29712–29723.
28. Yen, T. H., Chun, H.M., Tien, T. L., Lin, L.W., Tzu, C.Y., Wen, H.C. Yung, C.C., Yung, Y.T., Krishna, P.P., Wei, T.H., Edward, Y.C. Layered MoS_2 Grown on c-sapphire by Pulsed Laser Deposition. Phys. *Status Solidi RRL* **2015**, 9, 187-191.
29. Zhan, B., Butt, S., Liu, Y., Lan, J. Le, Nan, C.W., Lin, Y.H. High-Temperature Thermoelectric Behaviors of Sn-doped n-type Bi_2O_2Se ceramics. *J. Electroceramics* **2015**, 34, 175–179.
30. Dai, H., Lü, W., Zuo, X., Zhu, Q., Pan, C., Niu, X., Liu, J., Chen, H.L., Chen, X. A novel Biosensor Based on Boronic Aacid Functionalized Metal-organic Frameworks for the Determination of Hydrogen Peroxide Released from Living Cells. *Biosens. Bioelectron.* **2017**, 95, 131–137.
31. Anna, P., Justyna, W., Tomasz, S., Michal, W., Robert, C.T., Andrzej, T.S., Michal, A.Z. Vitamin D Derivatives Enhance Cytotoxic Effects of H_2O_2 or Cisplatin on Human Keratinocytes. *Steroids.* **2016**, 110, 49–61.
32. Balamurugan. T.S.T., Mani. V., Hsieh. C.C., Huang. S.T., Peng. T.K., Lin. H.Y. Real-time Tracking and Quantification of Endogenous Hydrogen Peroxide Production in Living Cells Using Graphenated Carbon Nanotubes Supported Prussian Blue Cubes. *Sens.Actuator B-Chem*. **2018**, 257, 220–227.

33. Vilian, A.T. E., Chen, S.M., Lou, B.S. A Simple Strategy for the Immobilization of Catalase on Multi-Walled Carbon Nanotube/poly (L-lysine) Biocomposite for the Detection of H_2O_2 and Iodate. *Biosens. Bioelectron.* 2014, 61, 639-647.
34. Vilian, A.T.E., Chen, S.M., Kwak, C.H., Hwang, S.K., Huh, Y.S., Han, Y.K., Immobilization of Hemoglobin on Functionalized Multi-Walled Carbon Nanotubes-Poly-l-Histidine-Zinc Oxide Nanocomposites Toward the Detection of Bromate and H_2O_2. *Sens.Actuator B-Chem.* **2016**. 224, 607-617.
35. Tarvin, M., McCord, B., Mount, K., Sherlach, K., Miller, M.L. Optimization of two methods for the Analysis of Hydrogen Peroxide: High performance Liquid Chromatography with Fluorescence Detection and High Performance Liquid Chromatography with Electrochemical Detection in Direct Current Mode. *J Chromatogr A* **2010**, 1217, 7564–7572.
36. Steinberg, S.M. High Performance Liquid Chromatography Method for Determination of Hydrogen Peroxide in Aqueous Solution and Application to Simulated Martian Soil and Related Materials. *Environ Monit Assess* **2013**, 185, 3749–3757.

TOC

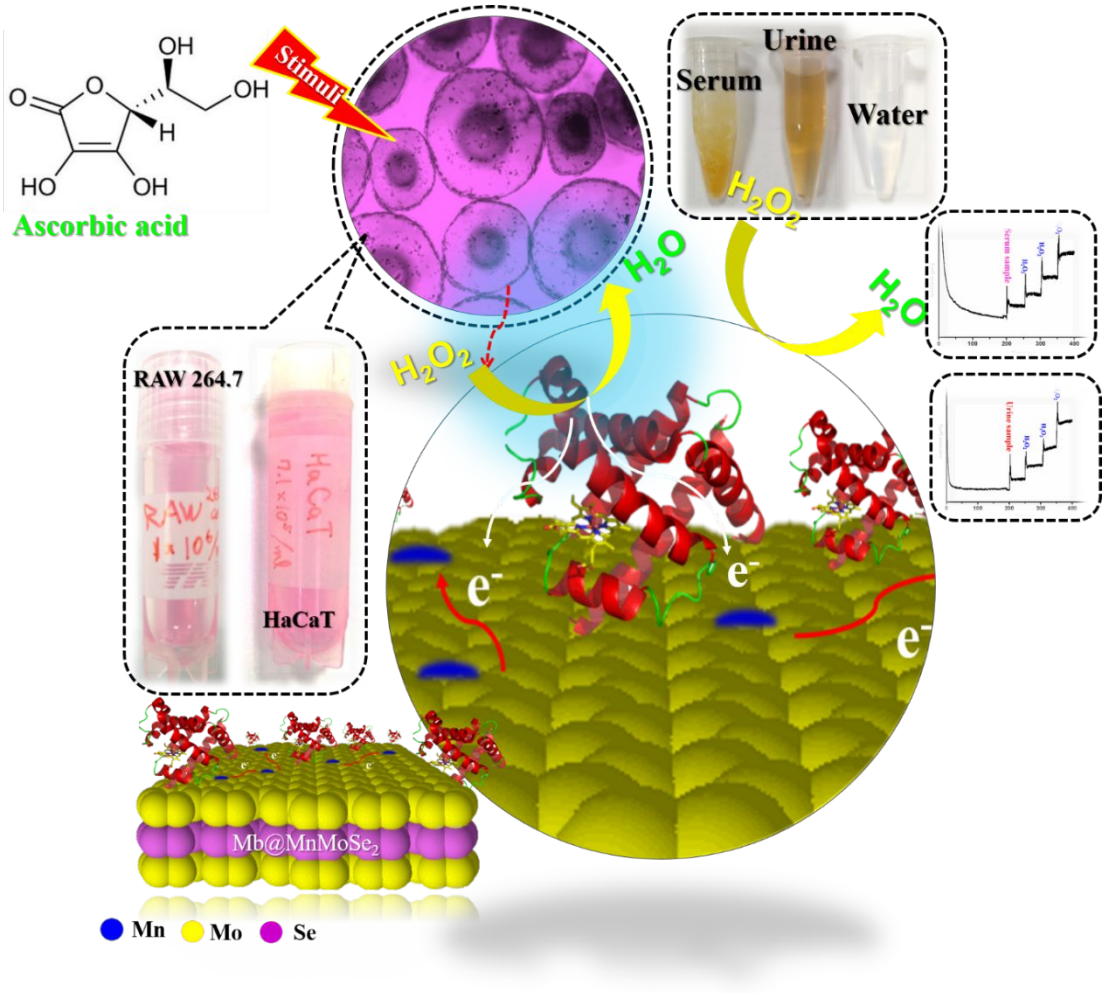
OH
O
O
OH
H
HO
OH
Ascorbic acid
Stimuli
Urine
Serum
Water
H_2O_2
H_2O
H_2O_2
H_2O
RAW 264.7
HaCaT
e⁻
e⁻
e⁻
Mb@MnMoSe$_2$
Mn
Mo
Se